The effects of operating conditions on the performance of a solid oxide steam electrolyser: a model-based study

Qiong Cai, Eduardo Luna-Ortiz, Claire Adjiman, Nigel Brandon

Fuel Cells

The effects of operating conditions on the performance of a solid oxide steam electrolyser: a model-based study

Journal:	*Fuel Cells*
Manuscript ID:	fuce.200900211.R2
Wiley - Manuscript type:	Original Research Paper
Date Submitted by the Author:	08-Jun-2010
Complete List of Authors:	Cai, Qiong; Imperial College London Luna-Ortiz, Eduardo; Imperial College London Adjiman, Claire; Imperial College London Brandon, Nigel; Imperial College London, Energy Futures Lab
Keywords:	Hydrogen production, High temperature electrolysis, SOEC, Temperature distribution, Temperature control

The effects of operating conditions on the performance of a solid oxide steam electrolyser: a model-based study

Q. Cai [1], E. Luna-Ortiz [2], C. S. Adjiman [2] , N. P. Brandon[1, *]

[1] Department of Earth Science and Engineering, Imperial College London, SW7 2AZ, UK

[2] Centre for Process Systems Engineering, Department of Chemical Engineering, Imperial College London, SW7 2AZ, UK

Received

[*] Corresponding author, n.brandon@imperial.ac.uk

Abstract

To support the development of hydrogen production by high temperature electrolysis using solid oxide electrolysis cells (SOECs), the effects of operating conditions on the performance of the SOECs were investigated using a one-dimensional model of a cathode-supported planar SOEC stack. Among all the operating parameters, temperature is the most influential factor on the performance of an SOEC, in both cell voltage and operation mode (i.e. endothermic, thermoneutral and exothermic). Current density is another influential factor, in both cell voltage and operation mode. For the conditions used in this study it is recommended that the SOEC be operated at 1073 K and with an average current density of 10000 A m^{-2}, as this results in the stack operating at almost constant temperature along the cell length. Both the steam molar fraction at the inlet and the steam utilisation factor have little influence on the cell voltage of the SOEC but their influence on the temperature distribution cannot be neglected. Changes in the operating parameters of the SOEC can result in a transition between endothermic and exothermic operation modes, calling for careful temperature control. The introduction of air into the anode stream appears to be a promising approach to ensure small temperature variations along the cell.

Keywords: Hydrogen production, High temperature electrolysis, SOEC, Operating conditions, Cell voltage, Operation mode, Temperature distribution, Temperature control

Nomenclature

$c_{p,C}$, $c_{p,A}$, $c_{p,S}$, $c_{p,I}$	heat capacity of the cathode and anode gas streams, solid structure and interconnect (J.kg^{-1}.K^{-1})
C_{H_2}, C_{H_2O}, C_{O_2}, C_{N_2}	concentration of hydrogen, steam, oxygen and nitrogen in the cathode and anode gas streams (mol.m^{-3})
C_i	concentration of gas species *i* in the cathode and anode gas streams (mol.m^{-3})
C_i^0	concentration of gas species *i* at the cell inlet (mol.m^{-3})
$C_{H_2}^{TPB}$, $C_{H_2O}^{TPB}$, $C_{O_2}^{TPB}$	concentration of hydrogen, steam and oxygen at the triple phase boundary (mol.m^{-3})
$d_{h,C}$, $d_{h,A}$	hydraulic diameter of the cathode and anode gas channels (m)
$D_{eff,cathode}$, $D_{eff,anode}$	average effective diffusivity coefficient of the cathode and anode (m^2.s^{-1})
$E_{cathode}$, E_{anode}	activation energy for the exchange current density of the cathode and anode (J.mol^{-1})
$E_{electrode}$	activation energy for the exchange current density of an electrode (J.mol^{-1})
J_A	inlet flow rate of the anode streams (mol s^{-1})
F	Faraday's constant (C.mol^{-1})
h_C, h_A, h_S, h_I	height of the cathode and anode channels, and thickness of the solid structure and interconnect (m)
j	local current density (A.m^{-2})
$j_{0,cathode}$, $j_{0,anode}$	exchange current density of the cathode and anode (A.m^{-2})
$j_{0,electrode}$	exchange current density of an electrode (A.m^{-2})
$\bar{j}$	Average current density of an electrode (A.m^{-2})
k_C, k_A	convective heat transfer coefficient between the solid parts of the cell and the cathode and anode gas streams (J.m^{-2}.s^{-1}.K^{-1})
$k_{cathode}$, k_{anode}	pre-exponential factor for the exchange current density of the cathode and anode (Ω^{-1}.m^{-2})
$k_{electrode}$	pre-exponential factor for the exchange current density of an electrode (Ω^{-1}.m^{-2})
L	cell length (m)
Nu_C, Nu_A	Nusselt number of the cathode and anode gas streams
P_{O_2}	oxygen pressure in the anode gas stream (Pa)
$P_{O_2}^{TPB}$	oxygen pressure at the triple phase boundary (Pa)
R	reaction rate (mol.s^{-1}.m^{-2})
R_{Ohm}	total resistance of the cell including electric and ionic resistances (Ω.m^2)
$\Re$	gas constant (J.mol^{-1}.K^{-1})
t	time (s)
T	temperature (K)
T_C, T_A, T_S, T_I	temperature of the cathode and anode gas streams, solid structure and interconnect (K)

T_C^0	temperature of the cathode gas stream at the inlet (K)
u_C, u_A	velocity of the cathode and anode gas streams (m.s^{-1})
U	cell potential (V)
U^0	standard potential (V)
U^{rev}	reversible potential (V)
$U^{rev,TPB}$	reversible potential estimated for the gas concentrations at the triple phase boundary (V)
W	cell width (m)
x	axial coordinate (m)
y_{O_2}	mole fraction of oxygen in the anode gas streams
α	transfer coefficient
ε_S, ε_I	emissivity of the solid structure and interconnect
$\eta_{act,cathode}$, $\eta_{act,anode}$	activation overpotential losses at the cathode and anode (V)
η_{conc}	total concentration overpotential losses (V)
$\eta_{conc,cathode}$, $\eta_{conc,anode}$	concentration overpotential losses at the cathode and anode (V)
η_{Ohm}	Ohmic losses (V)
η_{total}	total irreversible losses (V)
λ_C, λ_A, λ_S, λ_I	thermal conductivity of the cathode and anode gas streams, solid structure and interconnect (J.m^{-1}.s^{-1}.K^{-1})
ν_i	stoichiometric coefficient of gas species *i*
ν_{O_2}	stoichiometric coefficient of gas species *i*
ρ_C, ρ_A, ρ_S, ρ_I	density of the cathode and anode gas streams, solid structure and interconnect (kg.m^{-3})
σ	Stefan-Boltzmann constant (W.m^{-2}.K^{-4})
$\sigma_{cathode}$, σ_{anode}	electric conductivity of the cathode and anode (Ω^{-1}.m^{-1})
$\sigma_{electrolyte}$	ionic conductivity of the electrolyte (Ω^{-1}.m^{-1})
$\tau_{cathode}$, $\tau_{electrolyte}$, τ_{anode}	thickness of the cathode, electrolyte and anode (m)
ψ	air ratio

1 Introduction

High temperature (HT) electrolysis is an attractive alternative to the conventional low temperature water electrolysis process. A combination of favourable thermodynamics and kinetics at high temperature (500-1000 °C), offers reduced electrical energy consumption per unit of hydrogen compared to low temperature water electrolysis, and thus may provide a cost-effective route to hydrogen production. This approach is particularly advantageous if a HT electrolyser may be simply and efficiently coupled to a source of renewables (solar [1, 2], geothermal [3, 4] and wind [2]) or nuclear [5] electrical energy, to produce carbon-free hydrogen. A number of studies [1-5] have shown that such coupled systems are technically feasible and economically viable.

HT electrolysis is performed using a solid oxide electrolysis cell (SOEC), which can be seen in simple terms as the reverse operation of a solid oxide fuel cell (SOFC), allowing the opportunity to apply recent technology developments in SOFCs to the field. An SOEC consists of a three-layer solid structure (composed of porous cathode, electrolyte and porous anode) and an interconnect plate. Steam is introduced at the cathode side of the solid structure where it is reduced into hydrogen, releasing oxide ions in the process. The oxide ions then migrate through the electrolyte to the anode where they combine to form oxygen molecules, releasing electrons. A number of repeating cells are then packed into a stack to achieve an adequate hydrogen production rate.

At the system level, cell and stack configurations are important. Although the single cells of an SOEC stack can be in either a tubular configuration or planar configuration, planar cell structures are most commonly used for SOECs due to their lower manufacturing cost, higher packing density, and significantly smaller hot volume in the system compared to tubular designs [7, 8]. The planar design also allows for shorter current paths, reducing the Ohmic resistance within the cell [9]. A planar SOEC can be categorised as being an electrolyte-supported, electrode-supported or metal-supported design. The electrolyte-supported design employs the electrolyte as the support structure and is suitable for high temperature operation at which the Ohmic resistance associated with a thick electrolyte can be reduced. In an electrode-supported cell one of the electrodes is the thickest part of the solid structure. A hydrogen electrode supported design has been developed in order to minimise Ohmic resistances in SOFCs operating at intermediate temperatures (600-800 ^{o}C) [10] and may also be applied to SOECs operating at intermediate or higher temperatures. Metal supported SOECs have also been studied by some researchers [11].

During the operation of an SOEC system, electrical energy is required as input for the electrolysis process. Only part of the electrical energy input is used for the electrolysis reaction whilst the other part is lost due to irreversible losses in the stack, which are transformed into heat. The stack temperature distribution is thus a compromise between the energy consumed by the electrolysis reaction and the heat generated, per mole of hydrogen produced. When the thermal energy generated by the irreversible losses exceeds that consumed by the reaction, the temperature is increased as the reaction proceeds along the stack, resulting in exothermic operation. In endothermic operation, the

heat generated via irreversible losses is lower than the thermal energy consumed by the reaction, which results in a temperature decrease as the reaction proceeds along the stack. Thermoneutral stack operation occurs when the thermal energy consumed by the reaction is precisely matched by the heat generated via irreversible losses. The operating mode depends on the operating conditions (such as stack temperature, average current density, operating voltage, steam utilisation and the inlet gas composition), as well as materials selection and cell and stack geometry. Temperature variations may occur during operation of the SOEC when one of the operating conditions changes. Therefore, a full understanding of how the operating conditions influence the performance of the SOEC stack is necessary to allow the response of the SOEC stack to be predicted.

As in SOFCs, the most common electrolyte material used in SOECs is yttria-stabilized zirconia (YSZ) which exhibits high oxygen ion conductivity and good mechanical strength. Proton conducting ceramics based on acceptor doped perovskites have also been investigated as candidate electrolyte materials for SOECs that operate at temperatures of 500-750 °C [6]. Typical materials for the cathode are nickel-YSZ cermets, and those for the anode are perovskite oxides such as lanthanum strontium manganite (LSM). There have to date only been limited studies on the use of alternative electrode materials for SOECS, and the reactions mechanisms are not fully understood [7]. Ceramics like those used in SOECs are typically brittle materials exhibiting little plasticity and low fracture toughness, and subjected to stresses that can arise from manufacturing (residual stresses), differences between thermal expansion coefficients, temperature gradients along the cell, oxygen activity gradients, and/or external mechanical loading. In general, a mixture of all these sources of stress is likely to be present and their magnitude depends on the properties of the materials, operating conditions, and design. During the normal operation of a SOEC, the suppression of temperature gradients or transients that can cause excessive stresses within the SOEC components and lead to cell breakdown is crucial. SOECs thus have specific advantages for continuous operation, e.g. when integrated with nuclear plants. When the operation of the SOEC is integrated with intermittent energy sources, the thermal cycling problem has to be overcome. Due to their intermittent nature, renewable energy resources – such as wind and solar energies – cannot produce power steadily, since their power production rates change with time. The development of an understanding of the response of the SOEC stack, especially its temperature profiles, to transient events that may occur during its operation with intermittent energy input is therefore essential before this technology can be deployed. The development of an appropriate control strategy over temperature fluctuations is also desirable.

In addition, SOEC technology faces challenges with materials corrosion, sealing, and start-up and shut-down issues. Despite this, the SOEC, as an alternative to alkaline and polymer-electrolyte-membrane electrolysers, has recently attracted increasing interest because it offers the benefit of lower electrical energy consumption per unit of hydrogen production. Studies of the experimental operation of SOECs can be found in several publications. Herring et al. [12] showed that the stack performance is dependent on the inlet steam flow rate based on the experimental measurement and modelling study

of a 10-cell stack. Schiller et al. [11] studied the electrochemical performance of an SOEC, and the structure of the materials at different temperatures and current densities, and tested the durability of the stack. Brisse et al. [13] paid special attention to the impedance behaviour of the SOEC operated at different temperatures, current densities and steam concentration. All these experimental studies of the SOEC (at the cell level and the stack level) are carried out in a furnace where the temperature is maintained at a constant level, although a temperature distribution within the stack has been reported [12].

A mathematical model is an important design tool for devices such as the SOEC, which are still in the development stage. It allows the prediction of the behaviour of the device under different process conditions, and assists in the optimisation of its performance as well as in the development of operational control policies. In particular, a model is essential for understanding the response of an electrolyser under steady electrical power input, such as those from the grid or nuclear energy, as well as under an intermittent renewable electrical power input, such as from renewables. There have been only a few modelling studies of SOECs reported. Ni et al. [14-16] developed a detailed model of gas transport in the electrode and their impact on the concentration over-potential. Hawkes et al. [17] reported the first 3 dimensional (3D) computational fluid dynamics (CFD) study of a 60-cell stack simulating planar solid oxide electrolysis cells (SOECs).

To capture the spatially-distributed stack performance (especially the temperature distribution during operation) and the transient behaviour of a stack when integrated with intermittent energy resources, we have developed a one-dimensional distributed dynamic model of a cathode-supported planar SOEC stack, with which some primary investigations on the operation of SOECs have been reported [18-20]. Steady state simulations using the model predicted an electricity consumption significantly less than that of low temperature electrolysers commercially available today [18]. The model also predicted the dependence of stack temperature distribution on the average current density (which is directly proportional to the H_2 production rate and related to the electricity input). To avoid significant thermal excursions in the stack, a temperature control strategy is employed in the model by introducing air flow at the anode side [20]. Such a control strategy could also aid in maintaining a constant operating mode for the stack, which is an important constraint as the system requirements vary depending on whether the stack is employed in an exothermic, endothermic or thermoneutral mode. Although SOEC systems are often considered for large scale steady state operation in which the input power source may be a nuclear reactor, temperature control becomes essential if the systems are to be used in dynamic operation with intermittent electrical power sources such as wind turbines or photovoltaic cells.

In this paper we use this previously-developed model to further investigate the effects of a wide range of operating conditions on the steady-state performance of the SOEC stack, with special emphasis on the spatial distribution of key stack performance indicators (e.g. temperature distribution along the stack). The aim of this study is to provide a deeper understanding of the steady-state

behaviour of an SOEC, and to identify a parametric window of operating conditions that offers efficient large-scale stack operation.

2 SOEC mathematical model

A previously developed one-dimensional dynamic model of a cathode-supported planar SOEC stack [18-20] is used to investigate the performance of such an electrolyser. The key features and assumptions of the model is presented in this section.

To ensure a sufficient rate of H_2 production, an SOEC system must consist of several repeating cells assembled in stacks. Models of such stacks are usually constructed by considering the smallest unit cell, which is assumed to describe the response of the whole stack subject to the use of adequate boundary conditions. Here, the modelled unit cell is considered to be in the centre of a sufficiently large stack, so that end effects are negligible. Although interconnects normally provide the gas flow channels above and below the solid structure, the effect of individual passages is here neglected. The pressure drop along the gas channels is also assumed negligible at the operating pressure of 0.1 MPa. For modelling purposes, the unit cell is considered to consist of four components, the cathode and anode gas streams, the solid structure (which includes the two electrodes – cathode and anode, and electrolyte) and the interconnect. A schematic view of such a unit cell is shown in Figure 1. The cathode stream inlet gas is composed of H_2 and H_2O. The addition of hydrogen in the cathode stream avoids the oxidation of materials that might be induced by using pure steam. Hydrogen can be recirculated from the cathode outlet. On the anode side, it is assumed that the produced oxygen flows out; no air is introduced. Figure 2 shows the same unit cell but with air flow being introduced at the anode side to enable temperature control of the stack. The two models are employed to compare the performance of the SOEC with and without temperature control. Such a comparison will be made in the results and discussions section.

The model developed consists of an electrochemical model, mass balances for the gas streams, and energy balances for the cathode and anode streams, solid structure and interconnect.

2.1 Electrochemical model

An electrochemical model is used to relate variables such as gas species concentrations, cell component temperatures and average current density to the electrical potential of the cell, which can then be used to calculate the electrical energy consumption. The electrical potential is taken as constant along the cell as the electrodes are assumed to be good electronic conductors. As shown in Eq. (1), the cell potential corresponds to the sum of the reversible potential and all the irreversible losses that occur as the electrical current is passed through the cell. Such irreversible losses include Ohmic losses, concentration overpotentials and activation overpotentials, which are all partly responsible for the heat produced within the cell.

$$U = U^{rev}(x) + \eta_{Ohm}(x) + \eta_{conc,cathode}(x) + \eta_{conc,anode}(x) + \eta_{act,cathode}(x) + \eta_{act,anode}(x) \quad (1)$$

The reversible potential is determined through the Nernst equation as Eq. (2), which predicts the minimum electrical potential required to split H_2O at a particular location along the cell with a specific temperature and gas concentration. Equation (2) has been derived assuming ideal gas behaviour. The solid structure temperature is applied in the Nernst equation as the reactions take place at the triple phase boundaries (TPBs) where the electrolyte, porous electrode and gas species meet at the interfaces between the electrolyte and the electrodes. U^0 represents the standard potential, which corresponds to the reversible potential calculated at unity activity. It is determined as a function of the Gibbs free energy change involved in the reaction, taking the partial pressures of H_2, H_2O and O_2 to be at standard pressure.

$$U^{rev}(x) = U^0(x) + \frac{\Re T_S(x)}{2F} \ln\left[\frac{C_{H_2}(x)[P_{O_2} \times 10^{-5}]^{0.5}}{C_{H_2O}(x)}\right] \quad (2)$$

Ohmic losses are linearly proportional to the current density and can be determined through Ohm's law as shown in Eq. (3), where j and R_{Ohm} represent the local current density and local cell resistance, respectively. R_{Ohm} is calculated using the conductivity data of each layer of the solid structure. In Eq. (4), cross plane charge flow and series connection of resistances have been assumed. The conductivity of the electrodes is assumed constant along the cell while that of the electrolyte is estimated as a function of local temperature.

$$\eta_{Ohm}(x) = j(x) R_{Ohm}(x) \quad (3)$$

$$R_{Ohm}(x) = \frac{\tau_{cathode}}{\sigma_{cathode}} + \frac{\tau_{electrolyte}}{\sigma_{electrolyte}(x)} + \frac{\tau_{anode}}{\sigma_{anode}} \quad (4)$$

Concentration gradients for the species develop in the porous electrode, if the fluxes of the reactant to, and the products away from, the TPBs are slower than that corresponding to the discharged electrical current. The cathode concentration overpotential is represented in Eq. (5). Equation (6) describes the anode concentration overpotential with air-fed anode channels. Note that the temperature of the gas mixture at the TPBs is represented by the solid structure temperature.

$$\eta_{conc,cathode}(x) = \frac{\Re T_S(x)}{2F} \ln\left[\frac{C^{TPB}_{H_2}(x) C_{H_2O}(x)}{C_{H_2}(x) C^{TPB}_{H_2O}(x)}\right] \quad (5)$$

$$\eta_{conc,anode}(x) = \frac{\Re T_S(x)}{4F} \ln\left[\frac{C_{O_2}^{TPB}(x) T_S(x)}{C_{O_2}(x) T_A(x)}\right] \quad (6)$$

The diffusion activities of H_2 and H_2O in the porous cathode are expressed in Eqs. (7) and (8), whilst the diffusion activity of O_2 in the porous anode is represented in Eq. (9). $D_{eff,cathode}$ represents the average effective diffusivity coefficients in the cathode, considering a binary gas mixture of H_2 and H_2O. $D_{eff,anode}$ represents the average effective diffusivity coefficient in the anode, considering a binary gas mixture of O_2 and N_2.

$$C_{H_2}^{TPB}(x) = C_{H_2}(x) + \frac{\tau_{cathode}}{2FD_{eff,cathode}} j(x) \quad (7)$$

$$C_{H_2O}^{TPB}(x) = C_{H_2O}(x) - \frac{\tau_{cathode}}{2FD_{eff,cathode}} j(x) \quad (8)$$

$$C_{O_2}^{TPB}(x) = C_{O_2}(x) + C_{N_2}(x) - C_{N_2}(x) \exp\left[\frac{-j(x)\tau_{anode}}{4FD_{eff,anode}[C_{O_2}(x) + C_{N_2}(x)]}\right] \quad (9)$$

Activation overpotentials are classically determined through the Butler-Volmer equation. Here the extended form of the Butler-Volmer equation is applied to account for the differences in the gas concentrations at the TPBs and in the bulk stream. Equations (10) and (11) are for the cathode and anode activation overpotentials respectively. Although reactions are generally rapid and activation overpotentials tend to be small at high temperatures, they can become the most significant form of irreversible losses as the operating temperature is reduced.

$$j(x) = j_{0,cathode}(x)\left[\frac{C_{H_2}^{TPB}(x)}{C_{H_2}(x)} \exp\left[\frac{2(1-\alpha)F}{\Re T_S(x)} \eta_{act,cathode}(x)\right] - \frac{C_{H_2O}^{TPB}(x)}{C_{H_2O}(x)} \exp\left[\frac{-2\alpha F}{\Re T_S(x)} \eta_{act,cathode}(x)\right]\right] \quad (10)$$

$$j(x) = j_{0,anode}(x)\left[\exp\left[\frac{2(1-\alpha)F}{\Re T_S(x)} \eta_{act,anode}(x)\right] - \frac{C_{O_2}^{TPB}(x)}{C_{O_2}(x)} \exp\left[\frac{-2\alpha F}{\Re T_S(x)} \eta_{act,anode}(x)\right]\right] \quad (11)$$

where α (usually taken to be 0.5), $j_{0,cathode}$ and $j_{0,anode}$ represent the transfer coefficient and the exchange current density for the cathode and anode, respectively. Electrode exchange current densities are expressed in Eq. (12) as a function of the pre-exponential factor and activation energy. Here it is assumed that in an SOEC, the forward and backward reactions at each electrode as well as the

electrode materials are the reverse of those in an SOFC. Hence the values used for k_{anode} and E_{anode} in previous SOFC studies [11] have been substituted into k_{anode} and E_{anode} in the SOEC model. The same assumption is used when assigning the values to the SOEC anode kinetic parameters. The parameters employed for the SOEC simulations are shown in Table 1.

$$j_{0,electrode}(x) = \frac{\Re T_S(x)}{2F} k_{electrode} \exp\left[\frac{-E_{electrode}}{\Re T_S(x)}\right] \quad (12)$$

$$electrode \in \{cathode, anode\}$$

In the model as shown in Figure 1, only the cathode concentration overpotential was included; anode concentration overpotential was not taken into account, on the basis that the difference between the O_2 concentration at the triple phase boundaries (TPBs) and that in the bulk streams is negligible as the O_2 is assumed to just flow out of the cell [18]. However, when air is introduced through the anode channels, as shown in Figure 2, such an assumption no longer necessarily applies and it becomes important to include not only the cathode concentration overpotential but also the anode concentration overpotential in the model [20]. In both models shown in Figure 1 and Figure 2, Ohmic loss and activation overpotentials for both cathode and anode are included.

2.2 Mass balance

The composition of the cathode stream evolves along the cell as the H_2 / H_2O mixture moves towards the outlet. Such a composition change is tracked in the model using the cathode stream mass balance (as shown in Eqs. (13)-(15)) predicting the H_2 and H_2O concentrations at each location along the channel [18]. In the model as shown in Figure 1, mass balance is not considered for the anode channel. It is assumed that any O_2 produced flows naturally out of the channels and thus there is no forced gas movement as in the cathode side. The anode stream is modelled as a flow of pure O_2 at constant pressure along the cell [18].

$$\frac{\partial}{\partial t}[C_i(x)] = -u_C \frac{\partial}{\partial x}[C_i(x)] + \frac{1}{h_C} v_i R(x), \quad i \in \{H_2, H_2O\} \quad (13)$$

$$C_i(0) = C_i^0, \quad i \in \{H_2, H_2O\} \quad (14)$$

$$R(x) = \frac{j(x)}{2F} \quad (15)$$

However, for the SOEC stack with air-fed anode channels, as shown in Figure 2, an anode stream mass balance must be introduced in the model because the compositions of the anode streams evolve

as the mixture of O_2 and N_2 travels towards the outlet [20]. Here, the anode stream mass balance (as shown in Eqs. (16) and (17)) predicts the O_2 and N_2 concentrations at each location along the stack.

$$\frac{\partial}{\partial t}[C_i(x)] = -u_A \frac{\partial}{\partial x}[C_i(x)] + \frac{1}{h_A} v_i R(x) \quad i \in \{O_2, N_2\} \tag{16}$$

$$C_i(0) = C_i^0, \quad i \in \{O_2, N_2\} \tag{17}$$

The cathode and anode stream velocities are assumed constant (i.e. negligible frictional pressure drops along the stack) and determined from the outlet flow rate of the streams.

2.3 Energy balances

In the energy balances, it is considered that the thermal fluxes between the gas streams and the solid parts of the cell are fully described by convection. The thermal fluxes along the solid parts of the cell are modelled using Fourier's law of heat conduction while radiative heat exchange is taken into account between the solid structure and interconnect. The entire enthalpy change of the reaction is assumed to occur in the solid structure. Mean density and mean heat capacity values are applied in the anode and cathode energy balances. These are calculated as spatial averages of all the values along the cell. The remaining gas and material properties are taken to be constant along the cell. The energy balances are included in both models shown in Figure 1 and Figure 2. Equations (18)-(27) describe all the heat conduction mechanisms considered in this work.

$$\frac{\partial}{\partial t}[T_C(x)] = -u_C \frac{\partial}{\partial x}[T_C(x)] + \frac{k_C}{\rho_C c_{p,C} h_C}[T_S(x) - T_C(x)] + \frac{k_C}{\rho_C c_{p,C} h_C}[T_I(x) - T_C(x)] \tag{18}$$

$$T_C(0) = T_C^0 \tag{19}$$

$$\frac{\partial}{\partial t}[T_A(x)] = -u_A \frac{\partial}{\partial x}[T_A(x)] + \frac{k_A}{\rho_A c_{p,A} h_A}[T_S(x) - T_A(x)] + \frac{k_A}{\rho_A c_{p,A} h_A}[T_I(x) - T_A(x)] \tag{20}$$

$$T_A(0) = \frac{T_s(0) + T_I(0)}{2} \tag{21}$$

$$\begin{aligned}\frac{\partial}{\partial t}[T_S(x)] = {} & \frac{\lambda_S}{\rho_S c_{p,S}} \frac{\partial^2}{\partial x^2}[T_S(x)] - \frac{k_C}{\rho_S c_{p,S} h_S}[T_S(x) - T_C(x)] - \frac{k_A}{\rho_S c_{p,S} h_S}[T_S(x) - T_A(x)] \\ & - \frac{2}{\rho_S c_{p,S} h_S}\left[\frac{\sigma[T_S(x)^4 - T_I(x)^4]}{1/\varepsilon_S + 1/\varepsilon_I - 1}\right] + \frac{1}{\rho_S c_{p,S} h_S}[-\Delta H(x) R(x) + j(x) U]\end{aligned} \tag{22}$$

$$\frac{\partial}{\partial x}[T_S(0)] = 0 \quad , \qquad \frac{\partial}{\partial x}[T_S(L)] = 0 \tag{23}$$

$$\frac{\partial}{\partial t}[T_I(x)] = \frac{\lambda_I}{\rho_I c_{p,I}} \frac{\partial^2}{\partial x^2}[T_I(x)] - \frac{k_C}{\rho_I c_{p,I} h_I}[T_I(x) - T_C(x)] - \frac{k_A}{\rho_I c_{p,I} h_I}[T_I(x) - T_A(x)] + \frac{2}{\rho_I c_{p,I} h_I}\left[\frac{\sigma[T_S(x)^4 - T_I(x)^4]}{1/\varepsilon_S + 1/\varepsilon_I - 1}\right] \tag{24}$$

$$\frac{\partial}{\partial x}[T_I(0)] = 0 \quad , \qquad \frac{\partial}{\partial x}[T_I(L)] = 0 \tag{25}$$

$$k_C = Nu_C \frac{\lambda_C}{d_{h,C}} \quad , \qquad k_A = Nu_A \frac{\lambda_A}{d_{h,A}} \tag{26}$$

$$d_{h,C} = \frac{2Wh_C}{W + h_C} \quad , \qquad d_{h,A} = \frac{2Wh_A}{W + h_A} \tag{27}$$

2.4 Temperature control

We have proposed to provide the temperature control for an SOEC stack through the manipulation of the air ratio. In Figure 2, the schematic view of a unit cell with air flow through the anode gas channel is shown. The inlet air compositions are assumed to be 21 mol % O_2 / 79 mol % N_2. The air ratio reflects the inlet flow rate of air in relation to the rate of reaction. It is defined as the ratio between the moles of O_2 contained in the inlet air flow to that produced in the unit cell, per unit time. Assuming that a minimum of 50 mol % N_2 in the anode streams at the stack outlet is required to limit the corrosion of metallic components, the lower bound for the air ratio can be selected to be as small as 0.4. The upper bound is assumed to be 14, namely the maximum air flow rate which can be supplied without incurring significant additional energy costs (which may be caused by, e.g. using air compression) [21]. The mathematical expression for the air ratio is shown in Eq. (28).

$$\psi = \frac{2Ff_A^0 y_{O_2}(0)}{\bar{j}LW\nu_{O_2}} \tag{28}$$

3 Simulation results and discussion

The system of partial differential and algebraic equations is solved via the finite difference method using gPROMS Model Builder 3.1.4. The model input parameters such as cell geometry and material properties are given in Table 2.

The selection of operating conditions for an SOEC can significantly influence the irreversible losses, altering the cell potential required for the electrolysis, and also the temperature in the stack. The range of operating conditions investigated in this paper is given in Table 2. The temperature range and the average current density range investigated are respectively 973 -1173 K and 2000 – 15000 A m^{-2}. Here, a range of steam molar fractions in the cathode stream, from 50% to 90%, are chosen to study the impact of the steam content in the inlet gas. Accordingly, the steam utilisation is varied from 50% to 90% to investigate its impact on the performance of the SOEC. The effect of temperature control on the performance of the SOEC is also investigated.

3.1 Effects of temperature

An important operation condition to be selected in the design of an SOEC is the operating temperature due to its impact on both thermodynamics and kinetics. The reversible potential and irreversible losses are illustrated as a function of temperature in Figure 3. This investigation is based on the model as shown in Figure 1 in which anode concentration overpotential is ignored. For this investigation, the inlet gas is kept as 90 mol % H_2O / 10 mol % H_2, while the steam utilisation is set at 80%. Due to the oxidising environment that pure steam would create at elevated temperatures, such a gas composition is not recommended for the cathode stream in an SOEC. Instead, conceptual system designs may consider the recirculation of some of the product hydrogen which is mixed with the steam at the inlet to ensure reducing conditions. Here, 10 mol % H_2 in the cathode inlet stream is assumed sufficient. The steam utilisation factor is the fraction of total inlet steam consumed by the reaction. A higher steam utilisation factor corresponds to a higher H_2 production rate from the same amount of steam. However, it is also important for the steam utilisation factor to be low enough to avoid a significant increase in the cathode concentration overpotential caused by steam starvation near the cell outlet. Here, a value of 80% is chosen.

As shown in Figure 3, the total cell voltage is decreased from around 1.31 to 1.22 V, over the temperature range of 973- 1173 K. This is mainly attributed to the decrease of the overall irreversible loss with increasing temperature. Except for the cathode concentration overpotential, which remains approximately constant, all the irreversible losses decrease with temperature. It is also clear from Figure 3 that activation overpotentials are the dominant irreversible losses. As expected from the thermodynamics, the reversible potential given by the Nernst equation (as indicated by Eq. (2)) increases with temperature from 0.96 to 1.0 V. The decrease of the overall irreversible loss exceeds the increase of the reversible potential, giving a decrease in the total cell potential with increasing temperature. The selection of the operating temperature must consider the operation cost associated with the electrical energy consumed by the stack. The operation cost accounts for the investment cost

involved in creating both a stack with the required thermal stability as well as the whole system that needs to operate at that specified temperature. If the use of external heat sources is considered, the temperature of such a heat source would also become an important factor. The effects of temperature on the operation of SOEC will be further revealed in the following sections.

3.2 Effects of average current density

The investigations in this section are based on the model as shown in Figure 1 in which no air is introduced to the anode stream. In Figure 4, the effects of average current density on the cell potential are shown. For this investigation, the inlet gas is kept as 90 mol % H_2O / 10 mol % H_2, while the steam utilisation is set at 80%. As Figure 4 shows, the cell potential increases with increasing average current density at the three different temperatures investigated, due to the increased irreversible losses. This behaviour is also reported by Ni et al. based on their electrochemical models [14]. The average current density is directly proportional to the H_2 production rate. Although a decreased current density allows a reduction in the cell potential and consequent decrease in electrical energy consumption, a low current density also results in a low H_2 production rate per unit cell area. Therefore, the selection of the current density at which the cell should be operated must consider the operating cost involved with the electrical energy consumption of the stack as well as the investment cost associated with the stack area required in supporting the specified H_2 production rate. Brisse et al. [13] have reported experimentally the achievement of high electrical-to-hydrogen energy conversion efficiencies at 10000 A m^{-2}. In our later investigations an average current density of 10000 A m^{-2} is used.

In Figure 5 the cathode stream temperature distribution along the cell for different average current densities at a temperature of 1073 K is shown. We see a large temperature drop from the inlet to the outlet at low current densities (such as 2000 A m^{-2} and 4000 A m^{-2}); the temperature distribution becomes more and more flat as the current density is increased – at a current density of 10000 A m^{-2}, the temperature along the cell is almost constant. From this study, it can be envisaged that considerable effort will be required to control the temperature along the stack in the presence of current density variations.

In Figure 6 the effect of average current density on temperature difference ΔT (ΔT = outlet temperature – inlet temperature) at three different inlet temperatures is shown. When the inlet temperature is 973 K, a transition from a positive ΔT (a temperature increase along the cell) to a negative ΔT (a temperature decrease along the cell) occurs at average current density of 2500 A m^{-2}, above which it is an exothermic operation and below an endothermic operation. At inlet temperatures of 1073 K, a negative ΔT, which indicates an endothermic operation, is seen at all average current densities investigated. Similar behaviour is observed when the inlet temperature is 1173 K. However, the temperature difference for the inlet temperature of 1073 K is much smaller than that of 1173 K; further increases in the average current density may lead to a transition from the endothermic operation to the exothermic operation.

Deleted: in Figure 4

3.2 Effects of steam molar fraction

In this section the effects of the steam molar fraction in the inlet on the cell voltage and the temperature difference ΔT are investigated, as shown in Figure 7 and Figure 8 respectively. The investigations in this section are based on the model as shown in Figure 1 in which no air is introduced to the anode stream. The steam molar fraction has a minor impact on the cell voltage, as shown in Figure 7; changing the steam content in the inlet gas from 50 % to 90 % causes less than 0.05 V change in the cell voltage over all the temperatures investigated. At 973 K, increasing the steam molar fraction from 50 % to 90 % results in the cell voltage falling from 1.39 V to 1.35 V, whilst increasing the steam molar fraction from 50 % to 90 % at 1073 K makes the cell voltage drop from 1.295 V to 1.285 V. This is because the reversible potential, governed by the Nernst equation, decreases with increasing steam concentration. However, at 1173 K, the cell voltage increases with increasing the steam molar fraction; an increase of 0.01 V in the cell voltage is observed when increasing the steam molar fraction from 50% to 90%. This phenomenon occurs due to the combined effect of high steam molar fraction and high temperature. While high steam concentrations reduce the cell potential, high temperatures can also increase the Nernst potential (in spite of the drop of the activation overpotentials with high temperatures). Therefore, the effects of higher temperature are more dominant than the effects of high steam concentration.

The impact of steam molar fraction on the temperature difference ΔT is not negligible, however, at a current density of 10000 A m^{-2}, as shown in Figure 8. When the inlet temperature is 973 K, the temperature difference ΔT is positive over the whole range of steam molar fractions investigated, indicating exothermic operation; when the inlet temperature is 1073 K, ΔT is positive at a steam molar fraction of less than 80% but negative at steam molar fraction of greater than 80%, denoting a transition from exothermic operation to endothermic operation. When the inlet temperature is 1173 K, ΔT is negative across the whole range of steam molar fractions investigated, indicating endothermic operation. Over the entire range of steam molar fractions studied, the stack temperature at the outlet drops as the steam molar fraction increases, which results in a drop in ΔT. The drop in the outlet temperature that the SOEC experiences (at any given inlet temperature) when increasing the steam concentration is due to the fact that more heat is being absorbed (since the electrolysis reaction is endothermic). Although it is evident from Figure 8 that a similar dependence of ΔT on the steam molar fraction is seen at all temperatures, operating at 973 K and 1173 K results in a bigger ΔT (~20-40 K) than operating at 1073 K (up to ~20 K). In this case, it might be favourable to operate the stack at 1073 K as fluctuations in the steam molar fraction would not produce severe thermal stresses in the stack, requiring less stringent control. We thus choose to operate the stack at 1073 K and set the inlet gas composition to be 10% H_2 / 90% H_2O for further investigations.

3.3 Effects of steam utilisation

Although a low steam utilisation factor is preferred from the perspective of stack efficiency, a reduction in the steam utilisation factor results in an increased cathode stream flow rate for a given H_2 production rate. In the system design, the selection of the steam utilisation factor must take into account the efficiency of the entire system as well as the added investment cost involved in accommodating the increased cathode stream flow rate. Also, the steam utilisation factor must be low enough to avoid a significant increase in the cathode concentration overpotential caused by steam starvation near the cell outlet.

As in the previous sections, the investigations in this section are based on the model as shown in Figure 1. In Figure 9 the cell potential is shown as a function of steam utilisation at different temperatures and different current densities. When operating at 973 K, the cell potential decreases with increasing steam utilisation over the entire current density range studied whilst, when operating at 1073 K and 1173 K, the cell potential increases with increasing the steam utilisation. The variation of the cell potential over the entire steam utilisation investigated is very small – 0.005 V at 973 K, 0.02 V at 1073 K, and 0.04 V at 1173 K.

In Figure 10 the temperature difference ΔT is shown as a function of steam utilisation at different temperatures and different current densities. It can be seen that temperature, current density and steam utilisation factors all co-determine the operating mode of the SOEC stack. Operating at 973 K sees typical exothermic behaviour (i.e. a positive ΔT) at all the average current densities studied here. Operating at a lower current density such as 5000 A m^{-2} gives a much smaller ΔT compared with operating at 10000 A m^{-2}, which indicates that it may be beneficial to operate at a lower current density at this temperature to extend stack lifetime. However, this needs to be compensated with the hydrogen production rate as a lower current density means a lower production rate. We also need to keep in mind that at 973 K, endothermic behaviour may be seen only at a current density of lower than 2500 A/m^2, as we have shown in Figure 6. On the other hand, operating at 1073 K and 1173 K sees typical endothermic behaviour (i.e. a negative ΔT) at all the current densities studied here, and a higher current density gives a smaller ΔT. A very small ΔT (~20 K at 50% steam utilisation and ~0 K at 90% steam utilisation) is achieved when operating at 1073 K and 10000 A m^{-2}, indicating that temperature control might not be necessary under these operating conditions. When operating at any of the three temperatures, and over the current densities investigated here, changing the steam utilisation from 50 % to 90 % resulted in a change of only 20 K in the outlet temperature. Over the range of current densities investigated here, an increase of ΔT with increasing steam utilisation is observed for operating at 973 K, while a decrease of ΔT with the increase of the steam utilisation factor is observed when operating at 1073 K and 1173 K.

The dependence of the cell potential and ΔT on steam utilisation at different operating temperatures can be explained by examining the evolution of the steam and hydrogen concentrations along the stack, as shown in Figures 11-13. The rate at which the concentration of hydrogen increases as steam is consumed varies with steam utilisation. At higher steam utilisations, the steam is

consumed more quickly so the point where the concentration of steam is overtaken by hydrogen is closer to the inlet. This happens at all the temperatures, as can be seen in Figures 11-13. At higher temperatures (1073 K and 1173 K), the reaction rate is much faster than that at lower temperatures (973 K), such that the concentration of hydrogen overtakes that of steam at points very close to the inlet. This creates larger overpotentials and thus generates more heat, which compensates the endothermic operation. Therefore, a higher steam utilisation (i.e. 90%) reduces the temperature difference at the outlet compared to a lower steam utilisation (i.e. 50%).

3.4 Effects of temperature control

The extent of the variations in temperature along the stack with changing operating conditions calls for strict temperature control if such a stack is to be successfully built and used, especially in dynamic operation. Although SOEC systems are often considered for large-scale steady-state operation in which the input power source may be a nuclear reactor, temperature control becomes essential if the systems are to be used in dynamic operation with intermittent electrical power sources such as wind turbines or photovoltaic cells. To prevent the fracture of delicate stack components during dynamic operation, significant thermal stresses in the stack need to be avoided by the implementation of an effective control strategy. Such a control strategy would also assist in maintaining a constant operating mode of the stack, which is an important constraint as the system requirements vary depending on whether the stack is employed in an exothermic, endothermic or thermo-neutral mode. In our previous publications [19, 20], we have shown effective temperature control by introducing air in the anode stream side and manipulating the air ratio to maintain the constant temperature along the stack. The same strategy is applied here to show the effects of using temperature control on the cell potential and the temperature distribution along the stack. This work was done using the model shown in Figure 2.

First, we examined a suitable air ratio for controlling the temperature. The temperature distribution along the SOEC stack with air-fed anode channels operated at average current densities of 5000 and 15000 A m^{-2} are respectively illustrated in Figures 14 and 15. The air ratio is varied between 0.4 and 14 while the inlet temperature is maintained at 1073 K. As can be seen from both figures, the increase in the air ratio causes the stack temperature to become more uniformly distributed, approaching the temperature of the inlet stream. This shows that an increase in the air ratio provides enhanced cooling for the stack during exothermic operation, and enhanced heating during endothermic operation, via the increase in the convective heat transfer between the cell components and air flow. For both Figures 14 and 15, approximately 80% of the reduction in ΔT that can be achieved by varying the air ratio from 0.4 to 14 is seen upon going from an air ratio of 0.4 to 7. As discussed in our previous paper [20], the advantages of a more uniform temperature distribution from the increased air flow must be offset against the extra energy required to generate the increased air mass flow rate. Therefore, an intermediate air ratio value of 7 was selected for subsequent investigations.

Temperature distributions along the SOEC stack at different operating conditions are shown in Figures 16-18. The initial temperature distributions without air flow are compared to the temperature distributions with air flow. In Figure 16 typical endothermic operation is seen at 1073 K and a current density of 7500 A m^{-2}. For all the steam utilisations studied here, the temperature at the outlet increases to become closer to the temperature at the inlet when using an air ratio of 7 to control the temperature. In Figure 17, endothermic operation is also at 1073 K and a current density of 10000 A m^{-2} but with a smaller temperature difference between the outlet and the inlet compared to those shown in Figure 16. In cases where the largest ΔT values are observed without air flow, as with the steam utilisation of 50%, 60% and 70%, the air flow reduces ΔT, whereas when a small ΔT is observed without air flow (i.e. less than 10 K), as with the steam utilisation of 80% and 90%, then the air flow has the reverse effect by bringing the temperature at the outlet to a value further from the temperature at the inlet, which is not desirable.

Finally, as shown in Figure 18, typical exothermic operation is seen at 1073 K and at current density of 15000 A m^{-2}; for all the steam utilisations studied here, the temperature at the outlet decreases to become closer to the temperature at the inlet when using an air ratio of 7 to control the temperature.

From this discussion, a conclusion can be drawn that introducing air at the anode side of the SOEC, with an air ratio of 7.0, is effective to control the temperature of the stack for most combinations of steam utilisations and average current densities at a temperature of 1073 K. In some cases, smaller air ratios (or no air) are required for effective operation. As a result, an air ratio of 7 can be used as design limit.

In Figure 19, the cell potentials at 1073 K as a function of steam utilisation are presented, comparing the two cases when the SOEC stack is operating with and without air flow, at different current densities. Over all the investigated current densities, the figure shows small variation in the cell voltage as steam utilisation is changed from 50% to 90%. At current densities of 5000, 7500 and 10000 A m^{-2}, the cell potential decreases significantly when air flow is introduced into the anode stream, compared with the cell potential without air flow in the anode stream; at a current density of 15000 A m^{-2} or above, the cell potential increases when air flow is introduced into the anode stream, compared with the cell potential without air flow. These phenomena are observed for all the steam utilisation levels investigated. This behaviour may be explained as follows. As shown in Figures 16-18, at 1073 K when the current densities are 5000, 7500 and 10000 A m^{-2}, the stack is under endothermic operation; introducing air flow to the anode stream increases the temperature and decreases the O_2 partial pressure, which both act to reduce the cell potential. However, when the current density is at 15000 A m^{-2} or above, the stack is under exothermic operation; here introducing air flow at the anode stream brings the temperature down and also decreases the O_2 partial pressure. The increases in cell potential arising from the decreased temperature offset in part the decrease in cell

potential due to the decreased O_2 partial pressure, which couple together to increase the overall cell potential.

4 Model validation

It is desirable to compare the model results with experimental results, as a way to test the reliability of the model predictions. However, such comparison is difficult. Firstly, there is very limited experimental data reported on SOECs. Although some data can be found in papers such as [11], [13] and [22], only voltage data are reported; there is no temperature distribution / gradient data. Secondly, a valid comparison has to be based on common set of materials and experimental conditions. Whilst it is relatively easy to match the geometry and operating conditions of the model to those used in experiments, achieving a common and defined set of materials properties is non-trivial. Materials properties used in the model such as electrode activation energy, exchange current density, ionic conductivity, effective diffusivity, etc. all have significant impact on the modelling results. These properties are not normally reported along with the experimental measurements of SOEC performance, and the measurements of some of them (e.g. exchange current density) are not yet well established.

Noting these caveats, we have compared our modelled cell voltage with those reported in the literature. Operating at 1073 K and 0.1 MPa, a cell voltage of about 1.18 V at current density of 3000 A m^{-2} is reported by reference [11] for metal supported cells composed of Ni/YSZ cathode, YSZ electrolyte and LSCF anode, 1.07 V at current density of 5000 A m^{-2} by reference [13] for a cathode supported cell composed of Ni/YSZ cathode, YSZ electrolyte and LSM anode, and 1.24 – 1.37 V at current density of 2000 A m^{-2} by reference [22] for scandia-stabilized zirconia electrolyte supported cells. The electrolyte supported cells give relatively higher cell voltage mainly due to the bigger ohmic loss in the thicker electrolyte. These data were measured with sweep gases (air or pure nitrogen) introduced in the anode stream. The most relevant experimental data for comparison with our modelling results are from reference [13], as both are for cathode supported cells and use the same cell materials, though the experimental data is for a single cell and therefore does not introduce the temperature gradients that would be expected at the stack level. Suitable modelling results for comparison are those at 1073 K and with air flow introduced in the anode stream. The cell tested in reference [13] is characterized by a thickness of 240, 8 and 40 μm for cathode, electrolyte and anode respectively, and an active area of 45 cm^2. These cell geometries are taken in our model. The material properties are kept as those in Table 1 and Table 2. Both the modelled and the experimental polarisation curves depict similar trends of increased cell voltage with current density with, for example, cell voltages of around 1.07 to 1.14 V predicted at 70% steam utilisation over the current density range 4000 to 8000 A m^{-2}, as compared to measured values of around 1.03 to 1.13 V under the same conditions.

The polarisation curve of a low temperature PEM electrolyser operated at 328 K and 1MP from reference [23] can also be compared to the model and experimental polarisation curves of an SOEC operated at 1073 K and 0.1 MP. At the same current density, the low temperature PEM electrolyser gives a much higher cell voltage, e.g. 0.7 – 1.0 V higher than those for SOEC. This means that to achieve the same hydrogen production rate, a low temperature electrolyser cell would require a higher electricity input, though final comparison requires further analysis at the complete system level.

5 Conclusions

A one-dimensional distributed dynamic model of a cathode-supported planar IT-SOEC stack has been employed to study the performance of an SOEC at various temperatures, current densities, steam molar fractions and steam utilisations. Among all the operating parameters, temperature is the most influential in determining the performance of an SOEC, in both cell voltage and in terms of its operating mode, i.e. exothermic, endothermic or thermoneutral, which is indicated by the temperature difference between the inlet and the outlet. Current density is another influential factor on both the cell voltage and operating mode of the SOEC; the cell potential increases with increasing average current density, whilst the extent of temperature variation along the cell depends on the inlet temperature. As the current density changes, the SOEC may go through the transition from endothermic to exothermic operation. From this study it is recommended to operate the SOEC at 1073 K and with the average current density of 10000 A/m^2, as such an operation leaves the stack operating at almost constant temperature along the cell.

The impact of the steam molar fraction on cell voltage is negligible, but it has a more significant impact on the temperature distribution along the cell. The stack temperature at the outlet drops as the steam molar fraction increases; at certain operating temperature, e.g. 1073 K, a change of steam molar fraction results in the transition from exothermic operation to endothermic operation. Hence, whilst the variation of the cell potential over the entire steam utilisation investigated is small, the impact of steam utilisation on the temperature difference between the inlet and the outlet cannot be neglected, given that changing steam utilisation from 50 % to 90 % results in a change of 20 K in the stack outlet temperature. Over the entire range of current densities investigated here, an increase of ΔT with an increase in the steam utilisation factor is observed when operating at 973 K, whilst a decrease of ΔT with an increase in the steam utilisation factor is predicted when operating at 1073 K and 1173 K.

The variation of temperature along the stack with operating conditions therefore calls for strict temperature control if such a stack is to be successfully built and used, especially in dynamic operation. The introduction of air flow at the anode stream side is suggested as a means to reduce temperature variation along the stack, by manipulating the ratio of air to O_2 produced to maintain a constant temperature along the stack. An air ratio of 7 has been found effective in controlling the temperature of the stack. However, if the temperature difference between the outlet and the inlet is smaller than 10 K, lower air ratios (or no air) should be used.

Acknowledgements

The authors are grateful for the support of the seventh framework of European Commission under the project RELHY ("Innovative solid oxide electrolyser stacks for efficient and reliable hydrogen production"), grant agreement 213009.

References

[1] J. Padina, T.N. Veziroglu, A. Shahin, *Int. J. Hydrogen Energy* **2000**, *25*, 295.

[2] S.H. Jensen, P.H. Larsen, M. Mogensen, *Int. J. Hydrogen Energy* **2007**, *32*, 3253.

[3] J. Sigurvinsson, C. Mansilla, B. Arnason, A. Bontemps, A. Maréchal, T.I. Sigfusson, F. Werkoff, *Energy Conversion and Management* **2006**, *47*, 3543.

[4] J. Sigurvinsson, C. Mansilla, P. Lovera, F.Werkoffa, *Int. J. Hydrogen Energy* **2007**, *32*, 1174.

[5] R. Elder, R. Allen, *Progress in Nuclear Energy* **2009**, *51*, 500.

[6] P.A. Stuart, T. Unnob, J.A. Kilner, S.J. Skinner, *Solid State Ionics* **2008**, *179*, 1120.

[7] M. Ni, M.K.H. Leung, D.Y.C. Leung, *Int. J. Hydrogen Energy* **2008**, *33*, 2337.

[8] R. Hino, K. Haga, H. Aita, K. Sekita, *Nuclear Engineering and Design* **2004**, *233*, 363.

[9] J. Larminie, A. Dicks, *Fuel Cell Systems Explained*, John Wiley & Sons, Chichester, **2003**, pp.216.

[10] P. Aguiar, C.S. Adjimana, N.P. Brandon, *J. Power Sources* **2004**, *138*, 120.

[11] G. Schiller, A. Ansar, M. Lang, O. Patz, *J. Applied Electrochemistry* **2009**, *39*, 293.

[12] J. S. Herring, J. E. O'Brien, C. M. Stoots, G. L. Hawkes, J. J. Hartvigsen, M. Shahnam, *Int. J. Hydrogen Energy* **2007**, *32*, 440.

[13] A. Brisse, J. Schefold, M. Zahid, *Int. J. Hydrogen Energy* **2008**, *33*, 5375.

[14] M. Ni, M.K.H. Leung, D.Y.C. Leung, *J. Power Sources* **2006**, *163*, 460.

[15] M. Ni, M.K.H. Leung, D.Y.C. Leung, *Electrochimica Acta* **2007**, *52*, 6707.

[16] M. Ni, M.K.H. Leung, D.Y.C. Leung, *Chemical Engineering Technology* **2006**, *29*, 636.

[17] G. Hawkes, J. O'Brien, C. Stoots, B. Hawkes, *Int. J.Hydrogen Energy* **2009**, *34*, 4189.

[18] J. Udagawa, P. Aguiar, N.P. Brandon, *J. Power Sources* **2007**, *166*, 127.

[19] J. Udagawa, P. Aguiar, N.P. Brandon, *J. Power Sources* **2008**, *180*, 46.

[20] J. Udagawa, P. Aguiar, N.P. Brandon, *J. Power Sources* **2008**, *180*, 354.

[21] P. Aguiar, C.S. Adjiman, N.P. Brandon, *J. Power Sources* **2005**, *147*, 136.

[22] J. E. O'Brien, C. M. Stoots, J. S. Herring, J. Hartvigsen, *J. Fuel Cell Science and Technology* **2006**, *3*, 213.

[23] F. Marangio, M. Santarelli, M. Calì, *Int. J.Hydrogen Energy* **2009**, *34*, 1143.

Tables

Table 1 Pre-exponential factor and activation energy for the exchange current density

$k_{cathode}$	6.54×10^{11} $\Omega^{-1}.m^{-2}$	$E_{cathode}$	1.40×10^{5} $J.mol^{-1}$
k_{anode}	2.35×10^{11} $\Omega^{-1}.m^{-2}$	E_{anode}	1.37×10^{5} $J.mol^{-1}$

Table 2 Model input parameters and operating conditions

Cathode channel height, h_C	0.001 m
Anode channel height, h_A	0.001 m
Solid structure thickness, h_S	570×10^{-6} m
Interconnect thickness, h_I	500×10^{-6} m
Cell length, L	0.4 m
Cell width, W	0.1 m
Cathode thickness, $\tau_{cathode}$	500×10^{-6} m
Electrolyte thickness, $\tau_{electrolyte}$	20×10^{-6} m
Anode thickness, τ_{anode}	50×10^{-6} m
Cathode electric conductivity, $\sigma_{cathode}$	80×10^{3} $\Omega^{-1}.m^{-1}$
Electrolyte ionic conductivity, $\sigma_{electrolyte}$	$33.4\times10^{3}\exp(-10.3\times10^{3}/T_S)$ $\Omega^{-1}.m^{-1}$
Anode electric conductivity, σ_{anode}	8.4×10^{3} $\Omega^{-1}.m^{-1}$
Cathode average effective diffusivity, $D_{eff,cathode}$	36.6×10^{-6} $m^2.s^{-1}$
Anode average effective diffusivity, $D_{eff,anode}$	13.7×10^{-6} $m^2.s^{-1}$
Solid structure emissivity, ε_S	0.8
Interconnect emissivity, ε_I	0.1
Solid structure heat capacity, $c_{p,S}$	500 $J.kg^{-1}.K^{-1}$
Interconnect heat capacity, $c_{p,I}$	500 $J.kg^{-1}.K^{-1}$
Solid structure thermal conductivity, λ_S	2 $J.m^{-1}.s^{-1}.K^{-1}$
Interconnect thermal conductivity, λ_I	25 $J.m^{-1}.s^{-1}.K^{-1}$
Solid structure density, ρ_S	5900 $kg.m^{-3}$
Interconnect density, ρ_I	8000 $kg.m^{-3}$
Cathode stream Nusselt number, Nu_C	3.09
Anode stream Nusselt number, Nu_A	3.09
Transfer coefficient, α	0.5
Cathode stream inlet temperature, T_C^0	973 – 1173 K

Steam molar fraction in cathode stream	50 – 90 % H_2O
Operating pressure	0.1×10^6 Pa
Average current density	5000 – 15000 $A.m^{-2}$
Steam utilisation factor	50 – 90 %

Figure Captions

Fig. 1 Schematic view of a unit cell of a planar SOEC stack. The case of co-flow is depicted.

Fig. 2 Schematic view of a unit cell of a planar SOEC stack with air flow through the anode gas channel. The case of co-flow is depicted.

Fig. 3 Reversible potential and irreversible losses as a function of temperature for an average current density of 5000 A m^{-2}. Inlet gas composition is taken as 90 mol % H_2O / 10 mol % H_2. Steam utilisation is 80%.

Fig. 4 Effect of current density on cell potential at a temperature of 973 K (dashed line), 1073 K (solid line) and 1173 K (dotted line). Inlet gas composition is 10% H_2 / 90% H_2O, and steam utilisation is 80%.

Fig. 5 Cathode stream temperature along the cell for average current densities of 2000, 4000, 6000, 8000 and 10000 A m^{-2}. Inlet gas composition is 10% H_2 / 90% H_2O. Inlet temperature is 1073 K. Steam utilisation is 80%.

Fig. 6 Effect of average current density on the temperature difference between the outlet and the inlet when the inlet temperature is 973 K (dashed line), 1073 K (solid line), and 1173 K (dotted line). Inlet gas composition is 10% H_2/90% H_2O, and steam utilisation is 80%.

Fig. 7 Effect of steam molar fraction on the cell potential at a current density of 10000 A m^{-2} and a temperature of 973 K (dashed line), 1073 K (solid line) and 1173 K (dotted line). Steam utilisation is fixed at 80%.

Fig. 8 Effect of steam molar fraction on the temperature difference ΔT at a current density of 10000 A m^{-2}, when the inlet temperature is 973 K (dashed line), 1073 K (solid line) and 1173 K (dotted line). Steam utilisation is fixed at 80%.

Fig. 9 Cell potential as a function of steam utilisation at different temperatures (dashed lines – 973 K, solid lines – 1073 K, dotted lines – 1173 K) and with different average current density (squares – 5000 A m^{-2}, circles – 7500 A m^{-2}, triangles – 10000 A m^{-2}).

Fig. 10 Temperature difference between the inlet and outlet of the SOEC stack as a function of steam utilisation when the inlet temperature is 973 K (dashed lines), 1073 K (solid lines), and 1173 K (dotted lines). Symbols indicate different average current densities (■ – 5000 A m^{-2}, ● – 7500 A m^{-2}, ▲ – 10000 A m^{-2}).

Fig. 11 Concentration of steam (dashed lines) and hydrogen (solid lines) along the stack, at an inlet temperature of 973 K and an average current density of 10000 A m^{-2}. The steam utilisation factors corresponding to each curve are marked in the figure.

Fig. 12 Concentration of steam (dashed lines) and hydrogen (solid lines) along the stack, at an inlet temperature of 1073 K and an average current density of 10000 A m^{-2}. The steam utilisation factors corresponding to each curve are marked in the figure.

Fig. 13 Concentration of steam (dashed lines) and hydrogen (solid lines) along the stack, at an inlet temperature of 1173 K and an average current density of 10000 A m^{-2}. The steam utilisation factors corresponding to each curve are marked in the figure.

Fig. 14 Cathode stream temperature along the stack for an average current density of 5000 A m^{-2}, steam utilisation of 80%, inlet temperature of 1073 K and air ratios of 0.4, 7 and 14.

Fig. 15 Cathode stream temperature along the stack for an average current density of 15000 A m^{-2}, steam utilisation of 80 %, inlet temperature of 1073 K and air ratios of 0.4, 7 and 14.

Fig. 16 Cathode stream temperature along the stack for an inlet temperature of 1073 K at an average current density of 7500 A m^{-2}. Solid lines indicate temperature distributions without air flow whilst dashed lines indicate temperature distributions with air flow in the anode stream at an air ratio of 7. The steam utilisation factors are marked in the figure, corresponding to each curve.

Fig. 17 Cathode stream temperature along the stack for an inlet temperature of 1073 K at an average current density of 10000 A m^{-2}. Solid lines indicate temperature distributions without air flow whilst dashed lines indicate temperature distributions with air flow in the anode stream at an air ratio of 7. The steam utilisation factors are marked in the figure, corresponding to each curve.

Fig. 18 Cathode stream temperature along the stack for an inlet temperature of 1073 K at average current density of 15000 A m^{-2}. Solid lines indicate temperature distributions without air flow whilst dashed lines indicate temperature distributions with air flow in the anode stream at an air ratio of 7.0. The steam utilisation factors are marked in the figure, corresponding to each curve.

Fig. 19 Cell potential as a function of steam utilisation at 1073 K and at different average current densities (squares – 5000 A m^{-2}, circles – 7500 A m^{-2}, triangles – 10000 A m^{-2}, diamonds - 15000 A m^{-2}). Filled symbols indicate the behaviour without air flow, whilst empty symbols indicate the behaviour with air flow in the anode stream using an air ratio of 7.

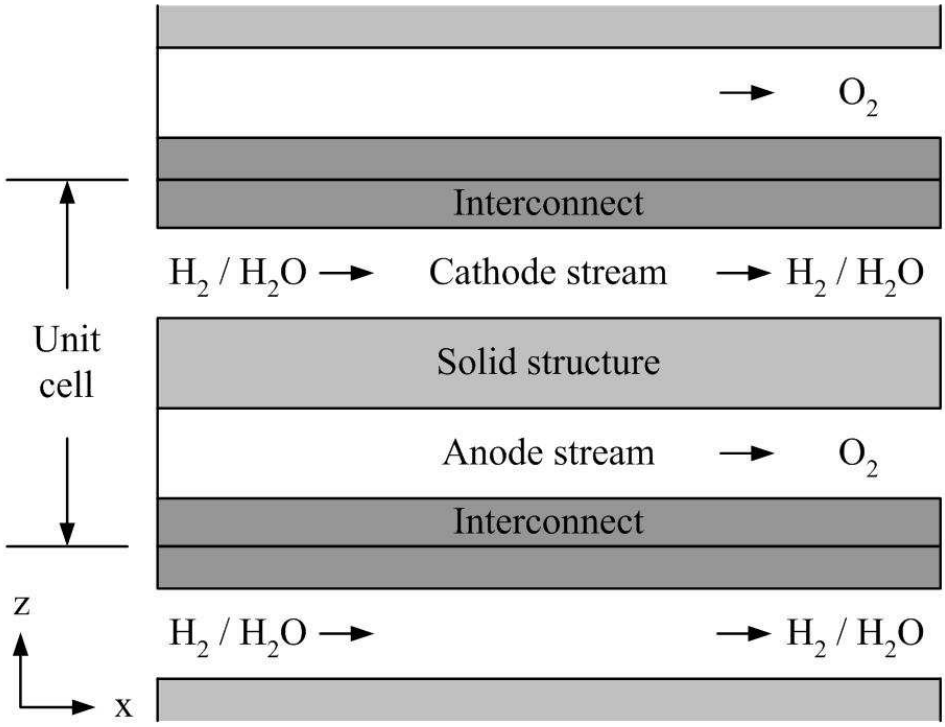

254x190mm (96 x 96 DPI)

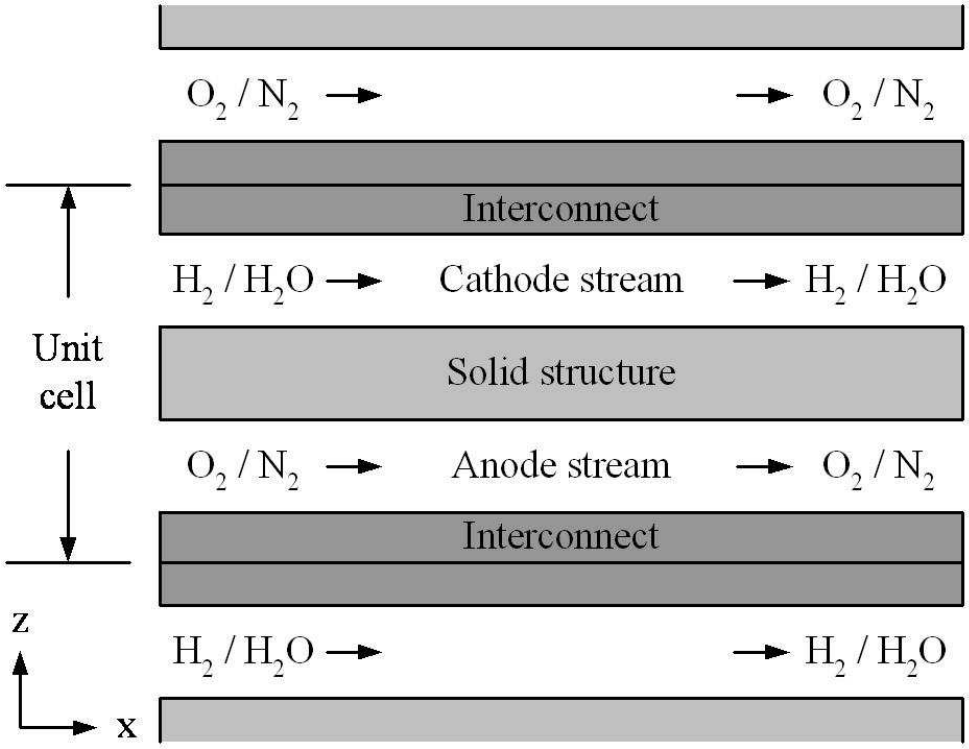

254x190mm (96 x 96 DPI)

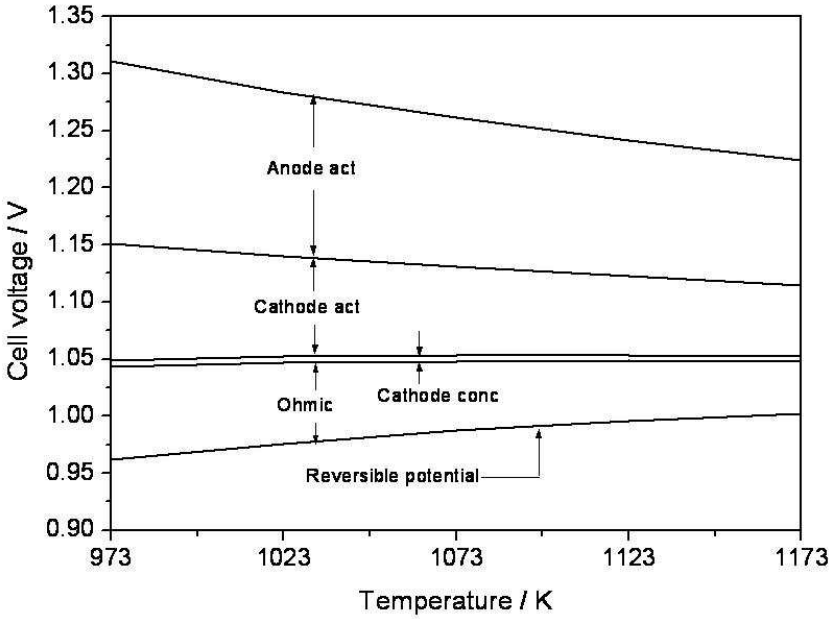

254x190mm (96 x 96 DPI)

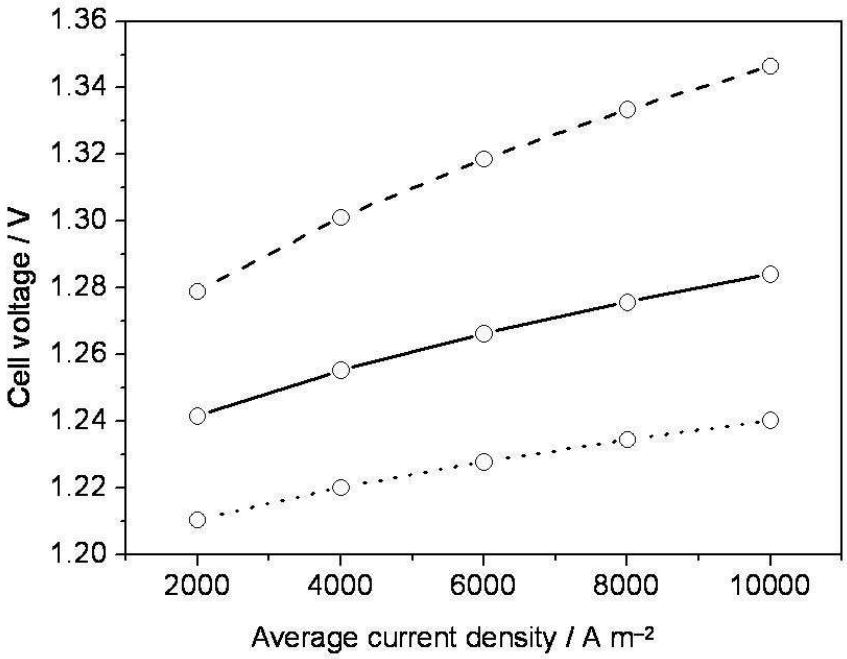

254x190mm (96 x 96 DPI)

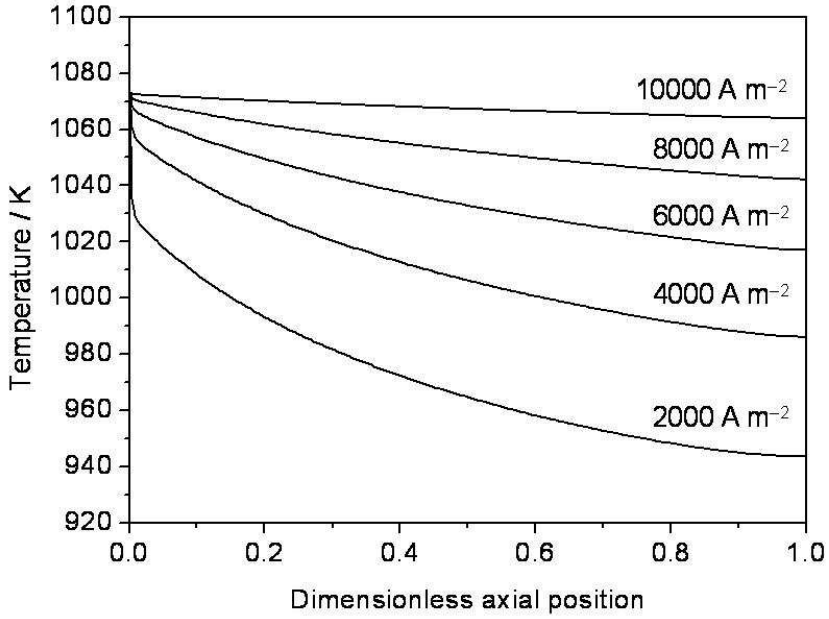

254x190mm (96 x 96 DPI)

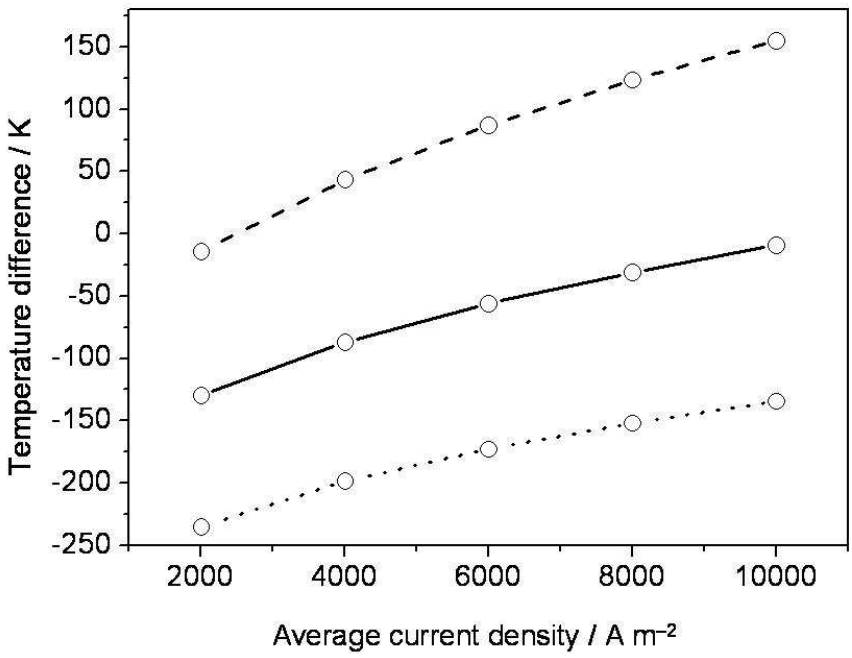

254x190mm (96 x 96 DPI)

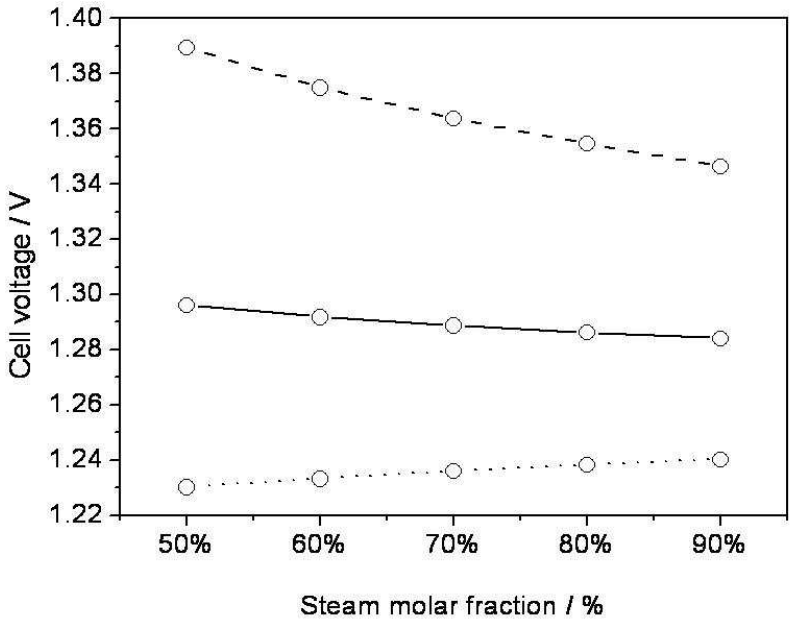

254x190mm (96 x 96 DPI)

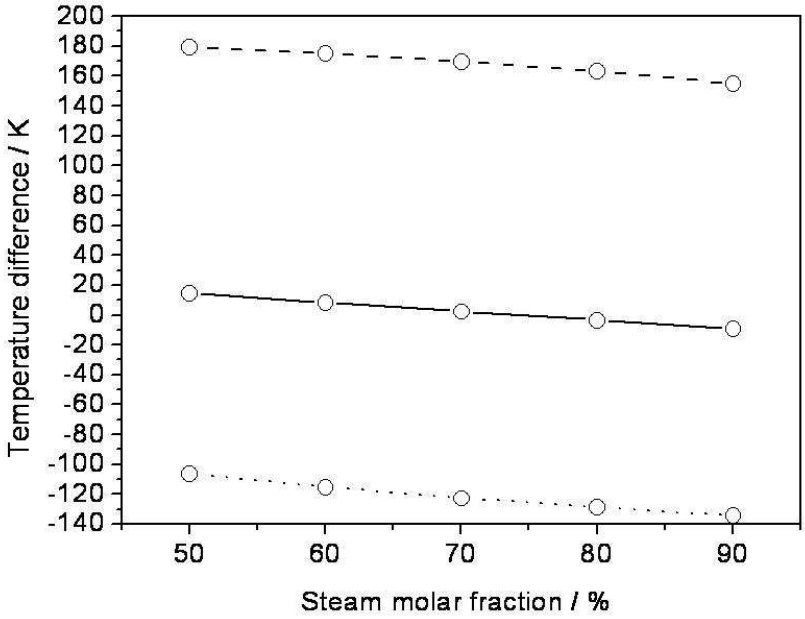

254x190mm (96 x 96 DPI)

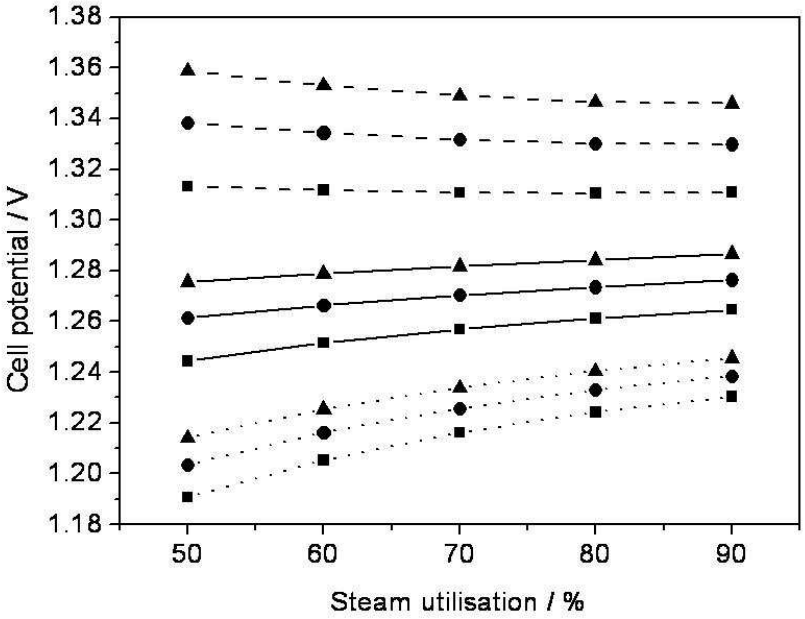

254x190mm (96 x 96 DPI)

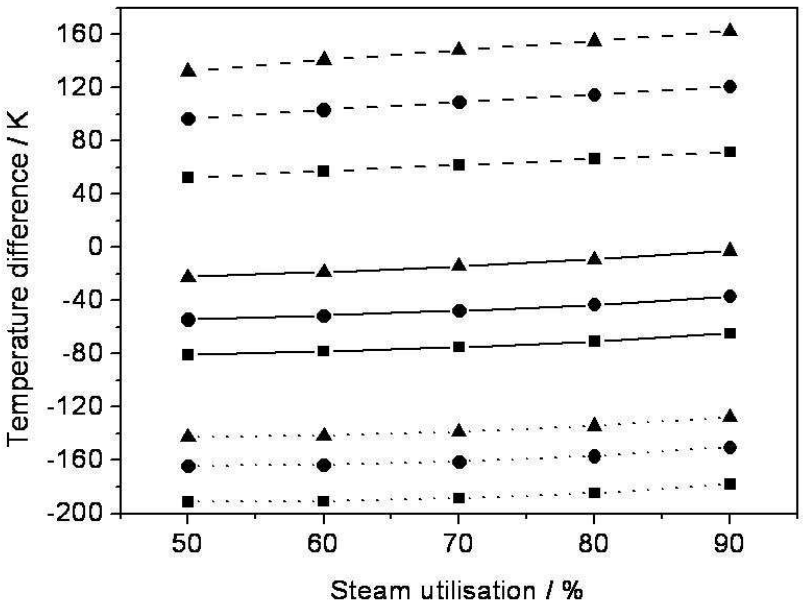

254x190mm (96 x 96 DPI)

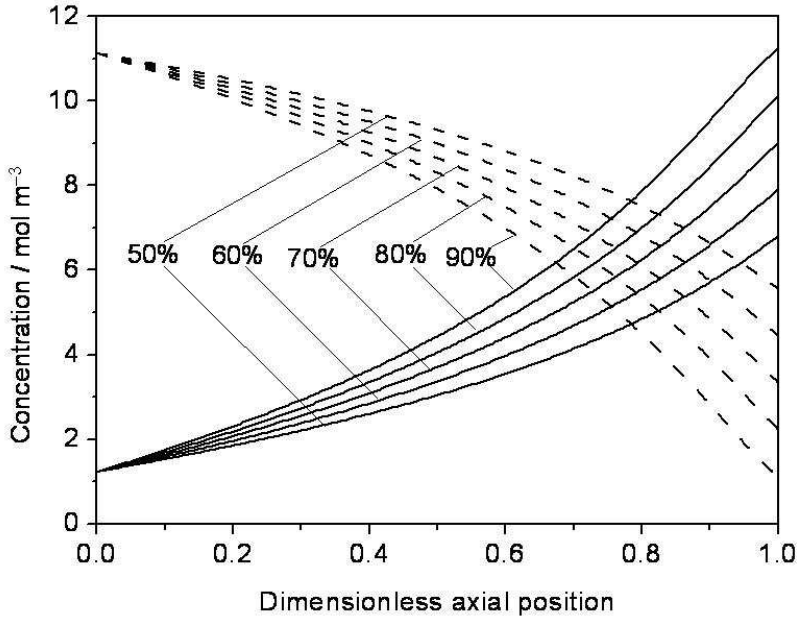

254x190mm (96 x 96 DPI)

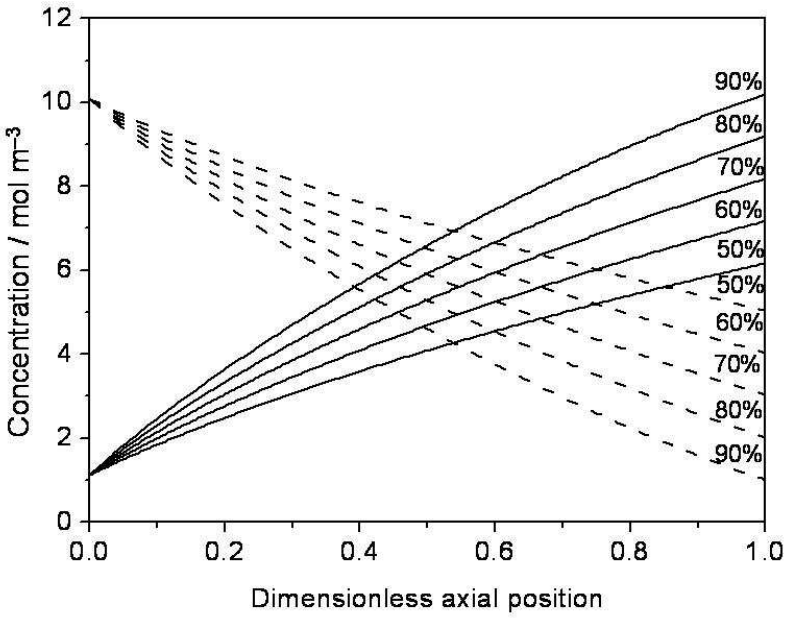

254x190mm (96 x 96 DPI)

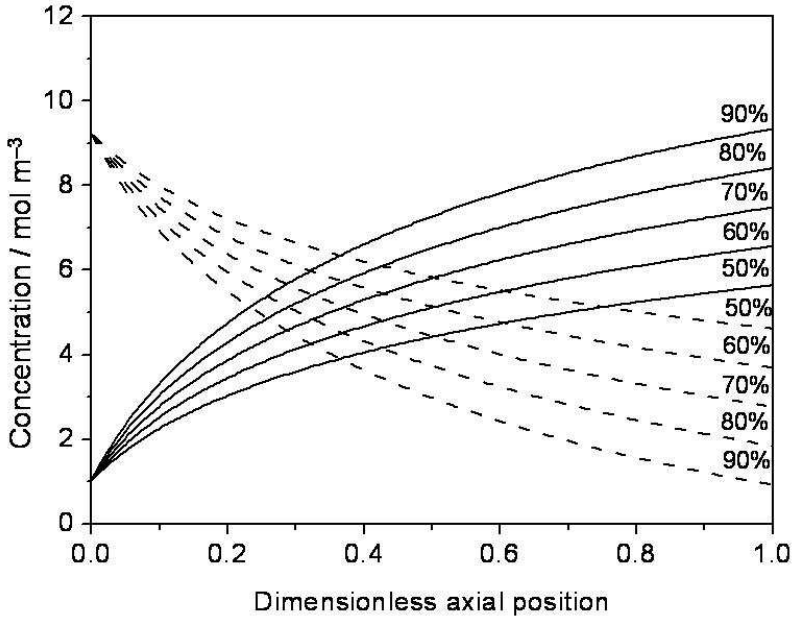

254x190mm (96 x 96 DPI)

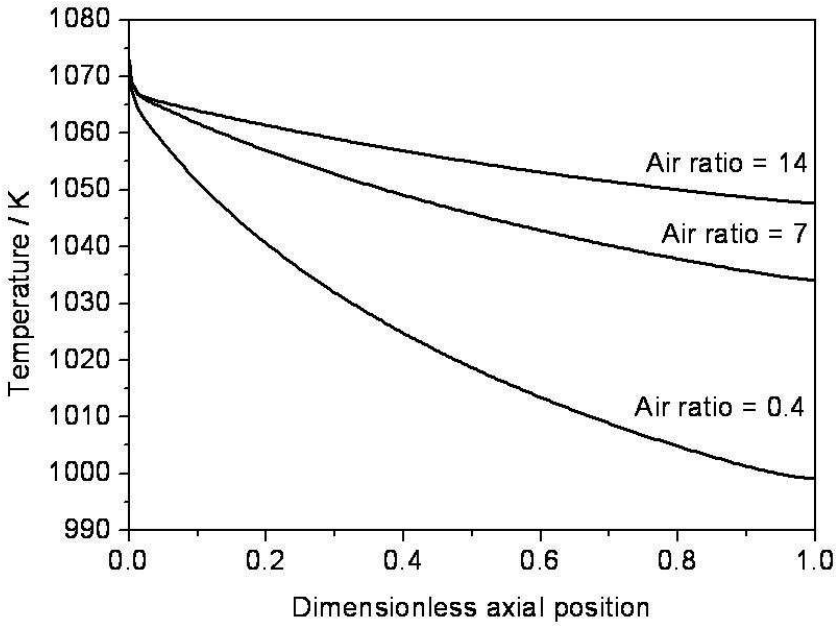

254x190mm (96 x 96 DPI)

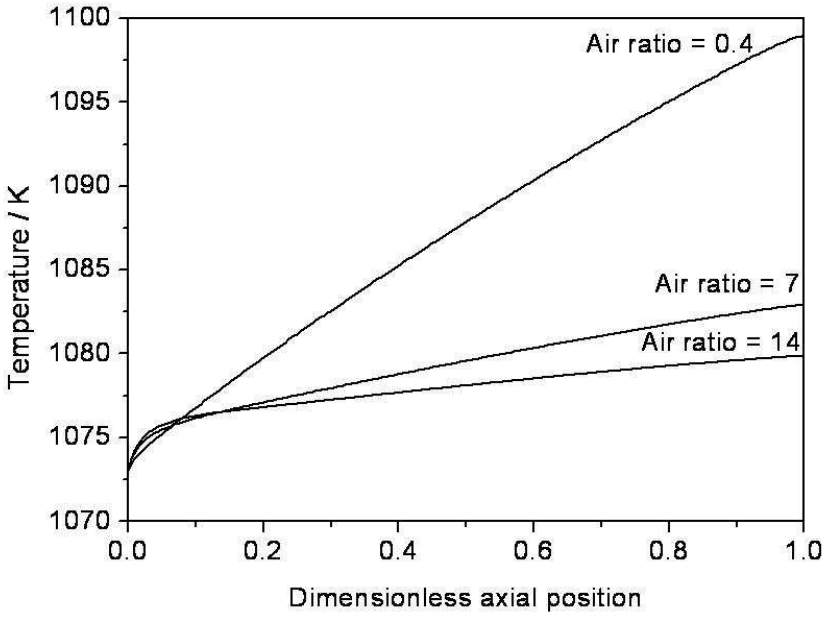

254x190mm (96 x 96 DPI)

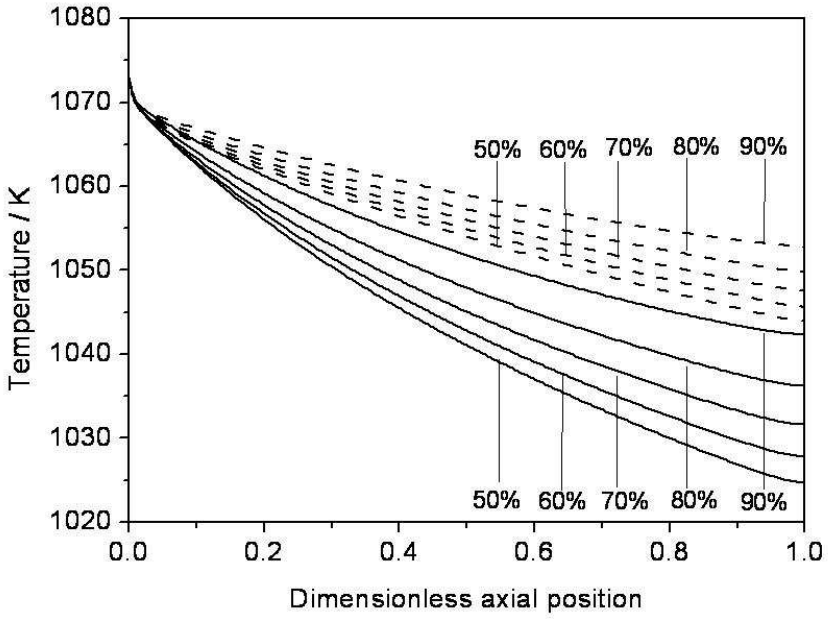

254x190mm (96 x 96 DPI)

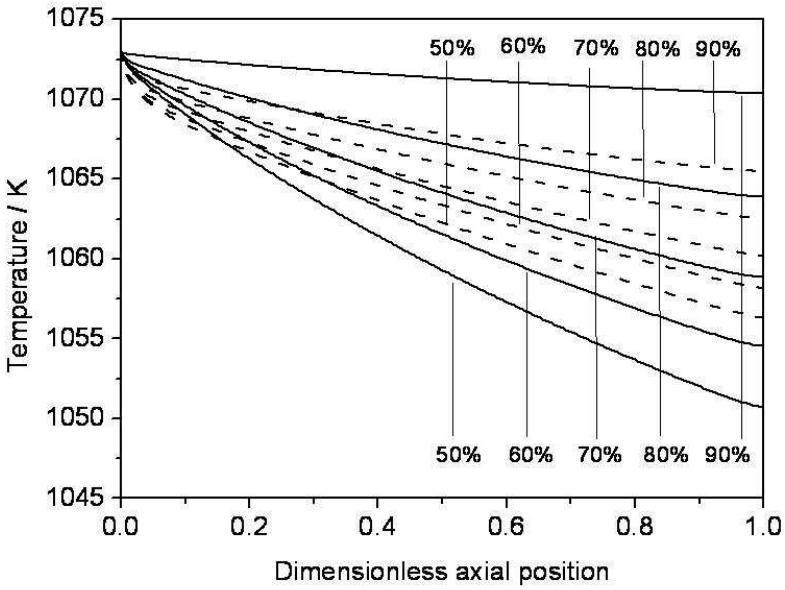

254x190mm (96 x 96 DPI)

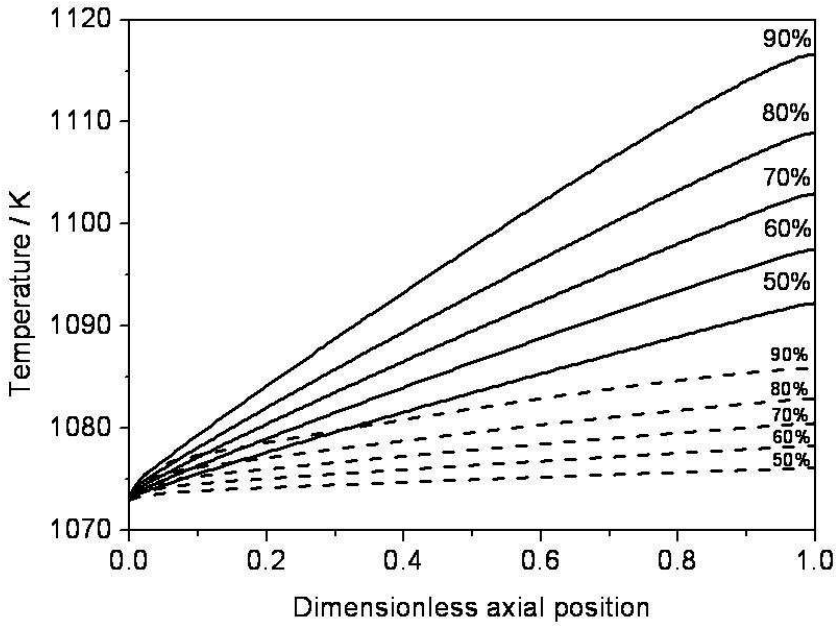

254x190mm (96 x 96 DPI)

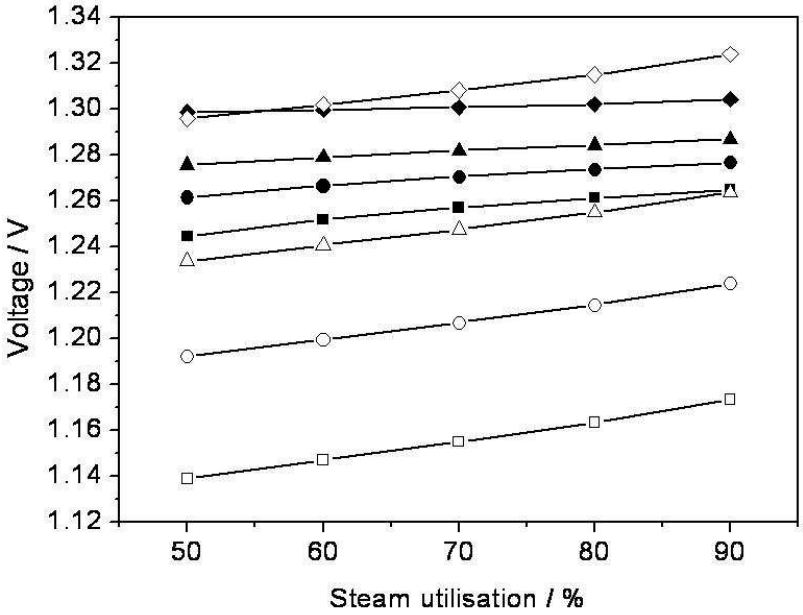

254x190mm (96 x 96 DPI)